Large-eddy simulation of a hypersonic turbulent boundary layer over a compression corner

Han Qi (齐涵); Xinliang Li (李新亮); Xiangxin Ji (纪相鑫); Fulin Tong (童福林); Changping Yu (于长平) ✉

Check for updates

View Online Export Citation

Large-eddy simulation of a hypersonic turbulent boundary layer over a compression corner

View Online   Export Citation   CrossMark

Han Qi (齐涵),[1,2] Xinliang Li (李新亮),[1,2] Xiangxin Ji (纪相鑫),[1,2] Fulin Tong (童福林),[3] and Changping Yu (于长平)[1,a]

AFFILIATIONS

[1] LHD, Institute of Mechanics, Chinese Academy of Sciences, Beijing 100190, China
[2] School of Engineering Science, University of Chinese Academy of Sciences, Beijing 100049, China
[3] Computational Aerodynamics Institute of China Aerodynamics Research and Development Center, Mianyang 621000, Sichuan, China

[a] Author to whom correspondence should be addressed: cpyu@imech.ac.cn

ABSTRACT

In this paper, large-eddy simulation of the interaction between a shock wave and the hypersonic turbulent boundary layer in a compression corner with a fixed $34°$ deflection angle at Ma = 6 for different Reynolds number cases is conducted. For investigating the effects of the Reynolds number for hypersonic cases, three cases where the free-stream Reynolds numbers are 14000, 20000, and 30000/mm are selected. The averaged statistics, such as the mean velocity, the skin friction, the heat flux, and the wall pressure, are used in this paper. The flow structures in the compression ramp including the shock wave and interaction region are discussed. The decomposition of the mean skin-friction drag for the flat flow is extended to be used in the compression corner. In addition, the turbulent kinetic energy is studied through the decomposition of the mean skin-friction drag for the flat-plate region and the corner region. It is found that higher Reynolds numbers would increase the turbulent kinetic energy by turbulent dissipation at the interaction region, while higher Reynolds numbers would decrease the turbulent kinetic energy by turbulent dissipation after reattachment. In addition, it is also found that the turbulent kinetic energy is larger with a higher Reynolds number and higher turbulent kinetic energy inhibits the movement from the separation point to the inflection point (x = 0 mm), which deduces larger separation bubbles.

I. INTRODUCTION

Shock wave/turbulent boundary layer interactions (STBLIs) are problems that are frequently faced by aircraft. In addition, they have a great impact on the aircraft layout and aerothermodynamic protection. There are various phenomena in the interaction flows, including the unsteady motion of the shock system, the separation and reattachment of the turbulent boundary layer, and the breathing motion of the separation bubble. For hypersonic aircraft, the local peak heat flow caused by the complex STBLI phenomenon in the corner can be tens of times of that in the case of no interactions, which will bring great threat to the flight safety of hypersonic aircraft. At present, STBLIs are basic problems for the design of the hypersonic aircraft and show great importance for engineering.[1,2]

There has been a lot of research that reported the mechanism of STBLIs.[3–5] The direct numerical simulation (DNS) was first used to explore the mechanism of compression ramp flow and oblique shock-wave/flat-plate boundary layer interaction flow by Admas[6] and Pirozzoli and Grasso,[7] respectively. Wu and Martin[8] also carried out DNS studies for compression ramp flows, where the incoming conditions are similar to those of wind tunnel experiments by Bookey et al.[9] Their studies show good agreement with the experimental results in terms of mean wall-pressure distribution, separation bubble length, and turbulent fluctuation amplification intensity. Wu and Martin[10] carried out some research about the shock wave low-frequency unsteadiness mechanism. Priebe et al.[11] also explored the shock wave low-frequency unsteadiness. The results of the DNS transition flows after low-pass filtering show that the low-frequency shock movement comes from the instability mechanism in the downstream sources of the separation bubble, and the expansion and contraction movement of the separation bubble leads to the low-frequency unsteadiness of the upstream sources. On this basis, Helm et al.[12] discussed in detail the spatial and temporal scale of the vortex structure in the shear layer of the separation bubble in the

interaction region. Fang et al.[13] proposed a new turbulence amplification mechanism. Li et al.[14] conducted the turbulent kinetic energy transport mechanism. For the length of the interaction region, Zheltovodov[15] studied its growth with an increasing ramp angle through a series of experiments at Ma = 3.0. Then both direct numerical simulation (DNS)[11] and large-eddy simulation (LES)[16] are carried out to study it. It was found that a larger Reynolds number produces a longer nondimensional interaction region. This conclusion is confirmed by another DNS study on a 25 deg ramp at Ma = 2.9.[17] Some new experimental research about the Reynolds number effect on the STBLI structure[18,19] is also carried out.

In general, previous studies were mainly carried out in the case of supersonic flows, while the studies of Reynolds number effects on the shock wave and turbulent boundary layer interaction in the hypersonic case are relatively few. Through the Reynolds-averaged Navier–Stokes equation numerical simulation (RANS), Feng-Yuan[20] carried out a study of ramp-induced planar shock-wave/turbulent boundary–layer interactions under hypersonic conditions. Stephan and Pino[21] conducted hypersonic STBLIs over an 8° compression ramp using DNS. The Reynolds number on the interaction between shock waves and turbulence at high Mach numbers will generate strong intrinsic compressible effects, also known as sound effects, referring to compressible effects related to turbulence fluctuations, which have a significant influence on physical quantities at different scales of turbulence. Further research on the flow mechanism of high Mach number shock waves and boundary layer interaction over the larger angle compression corner will help to further improve the understanding of this problem. In addition, large-eddy simulation (LES) is applied more to high Reynolds number cases successfully. Thus, in this paper, we perform an LES study of the hypersonic Mach 6.0 turbulent boundary layer over a compression corner of a 34° deflection angle.

II. GOVERNING EQUATIONS AND COMPUTATIONAL SETUP

A. Governing equations

By filtering the Navier–Stokes (N–S) equations, the filtered N–S equations for compression[22] in LES can be written as

$$\frac{\partial \bar{\rho}}{\partial t} + \frac{\partial \bar{\rho}\tilde{u}_j}{\partial x_j} = 0, \tag{1}$$

$$\frac{\partial \bar{\rho}\tilde{u}_i}{\partial t} + \frac{\partial \bar{\rho}\tilde{u}_i\tilde{u}_j}{\partial x_j} = -\frac{\partial \bar{p}}{\partial x_i} + \frac{\partial \tilde{\sigma}_{ij}}{\partial x_j} - \frac{\partial \tau_{ij}}{\partial x_j}, \tag{2}$$

$$\frac{\partial \bar{\rho}\tilde{E}}{\partial t} + \frac{\partial (\bar{\rho}\tilde{E} + \bar{p})\tilde{u}_j}{\partial x_j} = -\frac{\partial \tilde{q}_j}{\partial x_j} + \frac{\partial \tilde{\sigma}_{ij}\tilde{u}_i}{\partial x_j} - \frac{\partial C_P Q_j}{\partial x_j} - \frac{\partial J_j}{\partial x_j} + H, \tag{3}$$

$$\frac{\partial \bar{\rho}k_{sgs}}{\partial t} + \frac{\partial \bar{\rho}k_{sgs}\tilde{u}_j}{\partial x_j} = -\Pi_\Delta - \frac{\partial J_j}{\partial x_j} - \varepsilon_s + \varepsilon_d + \Pi_p + \frac{\partial \zeta}{\partial x_j} + \frac{\partial}{\partial}\left[\mu(\tilde{T})\frac{\partial k_{sgs}}{\partial x_j}\right], \tag{4}$$

where

$$\bar{\rho}\tilde{E} = \bar{\rho}C_v\tilde{T} + \frac{1}{2}\bar{\rho}\tilde{u}_i\tilde{u}_i + \bar{\rho}k_{sgs}, \tag{5}$$

$$\rho k_{sgs} = \frac{1}{2}\bar{\rho}(\widetilde{u_i u_i} - \tilde{u}_i\tilde{u}_i), \tag{6}$$

$$\tau_{ij} = \bar{\rho}(\widetilde{u_i u_j} - \tilde{u}_i\tilde{u}_j), \tag{7}$$

$$Q_j = \bar{\rho}(\widetilde{u_j T} - \tilde{u}_j\tilde{T}), \tag{8}$$

$$\tilde{q}_j = \frac{C_p\mu(\widetilde{T})}{P_r}\frac{\partial \tilde{T}}{\partial x_j}, \tag{9}$$

$$J_j = \frac{1}{2}\bar{\rho}(\widetilde{u_i u_i u_j} - \widetilde{u_i u_i}\tilde{u}_j), \tag{10}$$

$$\tilde{\sigma}_{ij} = 2\mu(\tilde{T})\widetilde{\mathbb{S}}_{ij}, \tag{11}$$

$$\widetilde{\mathbb{S}}_{ij} = \widetilde{S}_{ij} - \frac{1}{3}\delta_{ij}\widetilde{S}_{kk} = \frac{1}{2}\left(\frac{\partial \tilde{u}_i}{\partial x_j} + \frac{\partial \tilde{u}_j}{\partial x_i}\right) - \frac{1}{3}\frac{\partial \tilde{u}_k}{\partial x_k}\delta_{ij}, \tag{12}$$

$$H = -\varepsilon_d + \frac{\partial}{\partial x_j}\left[\mu(\tilde{T})\frac{\partial k_{sgs}}{\partial x_j}\right] + \frac{\partial}{\partial x_j}\left[\mu(\tilde{T})\frac{\partial}{\partial x_i}\left(\frac{\tau_{ij}}{\bar{\rho}}\right)\right], \tag{13}$$

$$\Pi_\Delta = \tau_{ij}\frac{\partial \tilde{u}_i}{\partial x_j}, \tag{14}$$

$$\varepsilon_s = 2\mu(\tilde{T})(\widetilde{\mathbb{S}_{ij}\mathbb{D}_{ij}} - \widetilde{\mathbb{S}}_{ij}\widetilde{\mathbb{D}}_{ij}), \tag{15}$$

$$\mathbb{D}_{ij} = \frac{\partial u_i}{\partial x_j} - \frac{1}{3}\delta_{ij}\frac{\partial u_k}{\partial x_k}, \tag{16}$$

$$\varepsilon_d = \frac{\partial}{\partial x_j}\left[\frac{5}{3}\left(\widetilde{\mu(\tilde{T})u_j\frac{\partial u_k}{\partial x_k}} - \mu(\tilde{T})\tilde{u}_j\frac{\partial \tilde{u}_k}{\partial x_k}\right)\right], \tag{17}$$

$$\Pi_p = \overline{p\frac{\partial u_k}{\partial x_k}} - \bar{p}\frac{\partial \tilde{u}_k}{\partial x_k}, \tag{18}$$

$$\zeta_j = \tau_{ij}\tilde{u}_i + \mu(\tilde{T})\frac{\partial}{\partial x_i}\left(\frac{\tau_{ij}}{\bar{\rho}}\right) + RQ_j. \tag{19}$$

In addition, $(\bar{\cdot})$ represents the spatial filtering with a low-pass filter at scale Δ, and $(\tilde{\cdot})$ represents the density-weighted (Favre) filtering $(\tilde{\phi} = \frac{\overline{\rho\phi}}{\bar{\rho}})$. For any flow variable, the spatial filtering of $\phi(x)$ can be denoted as

$$\bar{\phi}(x) = \int_\Omega G_\Delta(x,y)\phi(y)dy, \tag{20}$$

where $G_\Delta(x,y)$ is the kernel of the filter, which satisfies the normalization condition

$$\int_\Omega G_\Delta(x,y)dy = 1. \tag{21}$$

In this paper, the filter is a grid filter, with the filter width Δ being a measure of the local grid size.

In the filtered N–S equations, $\bar{\rho}$, $\tilde{u}_i$, $\tilde{T}$, $\tilde{p}$, and $\tilde{E}$ are the filtered density, velocity, pressure, and total energy, respectively. The filtered pressure is determined by $\tilde{p} = \bar{\rho}R\tilde{T}$, where R is the specific gas constant. In the equations, Pr is the molecular Prandtl number, and the molecular viscosity μ takes the form $\mu = \frac{1}{Re}\left(\frac{\tilde{T}}{\tilde{T}_\infty}\right)^{3/2}\frac{\tilde{T}_\infty + \tilde{T}_s}{\tilde{T} + \tilde{T}_s}$. According to Sutherland's law, in which Ts is 110.3 K, the Reynolds number Re takes the form $Re = \rho_\infty U_\infty L/\mu_\infty$. In Eqs. (1)–(4), k_{sgs}, τ_{ij}, Q_j, q_j, J_j, Π_Δ, ε_s, ε_d, and Π_p are the SGS kinetic energy, the SGS stress, the SGS heat flux, the heat flux, the SGS diffusion term, the SGS energy flux, the solenoidal dissipation, the dilatational dissipation, and the pressure dilatation, respectively.

For the unclosed terms, we choose the quasi-dynamic subgrid-scale kinetic energy equation model (QKM) proposed by Qi et al.[23] to model them. In the QKM, the subgrid-scale (SGS) stress can be expressed as

$$\tau_{ij}^{mod} = -2C_{sm}\bar{\rho}\Delta^2|\tilde{S}|\widetilde{\tilde{S}_{ij}} + \frac{2}{3}\delta_{ij}\bar{\rho}k_{sgs}, \tag{22}$$

where

$$|\tilde{S}| = \sqrt{2\tilde{S}_{ij}\tilde{S}_{ij}}, \tag{23}$$

$$C_{sm} = -\frac{\left(C_0\Delta_k^2\bar{\rho}\frac{\partial \tilde{u}_i}{\partial x_k}\frac{\partial \tilde{u}_j}{\partial x_k} - \frac{2}{3}\delta_{ij}\bar{\rho}k_{sgs}\right)\tilde{S}_{ij}}{2\bar{\rho}\Delta^2|\tilde{S}|\widetilde{\tilde{S}_{ij}}\tilde{S}_{ij}}, \tag{24}$$

$$C_0 = \frac{2k_{sgs}}{\Delta_l^2\frac{\partial \tilde{u}_k}{\partial x_l}\frac{\partial \tilde{u}_k}{\partial x_l}}. \tag{25}$$

The SGS heat flux can be expressed as

$$Q_j^{mod} = -\frac{\mu_{sgs}}{Pr_{sgs}}\frac{\partial \tilde{T}}{\partial x_j}, \tag{26}$$

where Pr_{sgs} is the SGS Prandtl number, and it can be solved in the QKM as

$$Pr_{sgs} = -\frac{\partial\left(\nu_{sgs}\frac{\partial \tilde{T}}{\partial x_j}\right)/\partial x_j}{\partial\left(C_0\Delta_k^2\frac{\partial \tilde{u}_j}{\partial x_k}\frac{\partial \tilde{T}}{\partial x_k}\right)/\partial x_j}. \tag{27}$$

The pressure diffusion term can be modeled as

$$\Pi_p \approx C_0\Delta_m^2\frac{\partial \tilde{p}}{\partial x_m}\frac{\partial^2 \tilde{u}_k}{\partial x_m \partial x_k}. \tag{28}$$

The solenoidal dissipation can be modeled as

$$\varepsilon_s \approx 2C_0\Delta_k^2\mu(\tilde{T})\frac{\partial\widetilde{\tilde{S}_{ij}}}{\partial x_k}\frac{\partial\widetilde{\mathbb{D}_{ij}}}{\partial x_k}. \tag{29}$$

The dilatational dissipation can be modeled as

$$\varepsilon_d \approx \frac{5}{3}\frac{\partial}{\partial x_j}\left[C_0\Delta_l^2\mu(\tilde{T})\frac{\partial \tilde{u}_j}{\partial x_l}\frac{\partial^2 \tilde{u}_k}{\partial x_k \partial x_l}\right]. \tag{30}$$

Differing from Ref. 23, all the unclosed terms from the filtered total energy equation are modeled (the term H is not neglected). Thus, this method can be applied to high compressible flows.
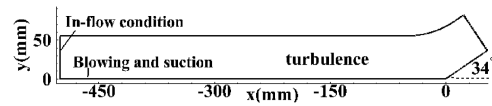

FIG. 1. Schematic diagram for the hypersonic turbulent boundary layer over a compression corner.

B. Computational setup

The LES is performed by using a high-order finite difference code OpenCFD-SC developed by Tong et al.,[24] and the governing equations are solved using the mixed scheme that includes CD6, WENO5, and WENO7[25] with a combination of absolute and relative limiters and the Steger–Warming splitting approach for the discretization of the convective flux terms. An eighth-order central difference scheme is used to compute the viscous flux terms. For STBLI flows, high-order spatial discretization schemes are necessary to resolve much finer turbulence structures and capture the separation region accurately. After all of the spatial terms are solved, the third-order Runge–Kutta method is used for time integration. Steady laminar boundary layer profiles are imposed at the inlet; a buff region with a coarse mesh is put in place to eliminate the disturbance reflection in the outlet region, and the flow variables are obtained using two-order downstream extrapolation at the outlet. Nonreflecting boundary conditions are used at the top boundary, and periodic boundary conditions are used in the spanwise direction. A no-slip boundary condition is used, with a constant wall temperature $T_w = 294$ K. The boundary condition is similar to that used in the study by Duan et al.[26] The fully developed incoming TBL is generated by the laminar-to-turbulent transition method used by Pirozzoli et al.[27] The same blowing and suction velocity disturbances are used to promote the transition in our LES. The blowing and suction velocity disturbance is imposed at -470 mm $< x < -440$ mm. Also, L (1 mm) is the non-dimensionalizing length scale. As shown in the sketch of the computational domain for simulation (Fig. 1), for the computational size, the streamwise direction is -550 to 54 mm, the wall direction is 55 mm, and the spanwise direction is 24 mm. The free-stream Mach number is 6. The free-stream temperature is

TABLE I. The main parameter and grid setting of the different cases.

Case	Grids	$Re_\infty/$mm
Case A	$2500 \times 400 \times 300$	14 000
Case B	$2800 \times 450 \times 350$	20 000
Case C	$2900 \times 500 \times 350$	30 000

TABLE II. The boundary layer parameters at x = −100 mm.

Case	Δx^+	Δy_{wall}^+	Δz^+	$\delta/$mm
Case A	7.3	0.32	4.01	9.9
Case B	11.56	0.42	6.35	8.8
Case C	15.91	0.50	8.79	8.3

79 K. Three cases of different Reynolds numbers are supplied. The main parameter and grid setting of the different cases are listed in Table I. The boundary layer parameters at x = −100 mm for different cases are shown in Table II.

III. VALIDATION

Before displaying and discussing the simulation results, the accuracy and reliability of the LES data should be validated. In this paper, the results are compared with equivalent data obtained in the incompressible regime according to Morkovin's hypothesis.[28] In this section, we show the profiles of root-mean-square (rms) from

different cases compared with the results from the study by Wu et al.[29] Figure 2(a)-2(c) show the rms from case A, case B, and case C, respectively. From the results, we can know that the rms in the streamwise direction, wall-normal direction, and spanwise direction is in good agreement with the results of the turbulent boundary layer on an incompressible plate[29] due to the non-dimensionalization of semi-local friction velocity. It is worth noting that in this paper, the spanwise direction is periodic and the spatial average is operated in the spanwise direction.

IV. RESULTS AND DISCUSSION

A. The averaged and instantaneous results

The wall-skin friction C_f and Stanton number S_t from different cases are shown in Figs. 3 and 4. From the figures, we can know that the separation bubble is larger as the Reynolds number increases. At $-440 < x/L < -300$, we see that the transition is developed for case B and case C but the transition of case A begins at $x/L = -300$.
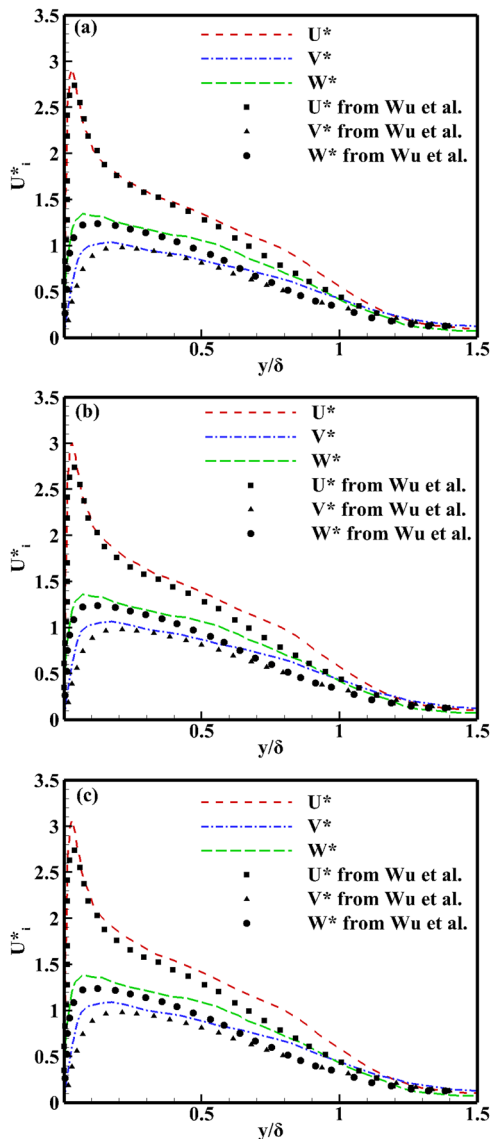

FIG. 2. Profiles of root-mean-square ($U_i = \sqrt{\rho/\rho_\infty}(u_i)^{rms}/u_\tau$). (a) is for case A; (b) is for case B; (c) is for case C.
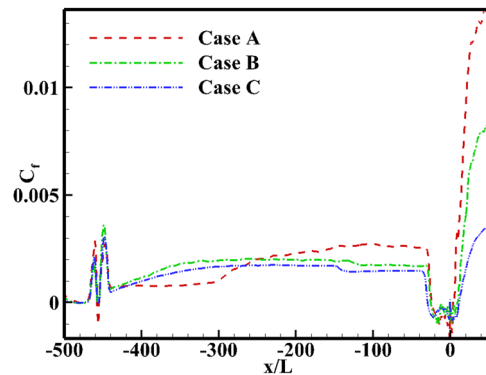

FIG. 3. Mean wall-skin friction C_f for different cases ($C_f = \mu_w (\frac{\partial \bar{u}}{\partial y})_w/(\frac{1}{2}\rho_\infty u_\infty^2)$).
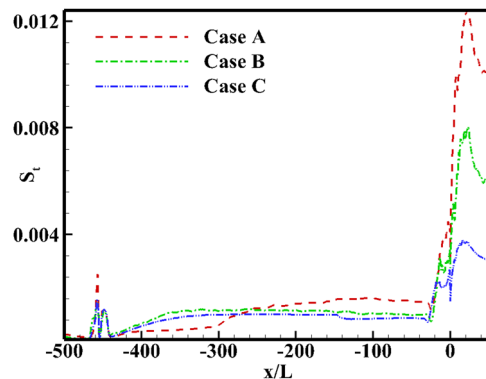

FIG. 4. Stanton number S_t for evaluating wall-heat flux from different cases ($S_t = k_w (\frac{\partial \bar{t}}{\partial y})_w/(\rho_\infty U_\infty C_p (T_0 - T_w))$).

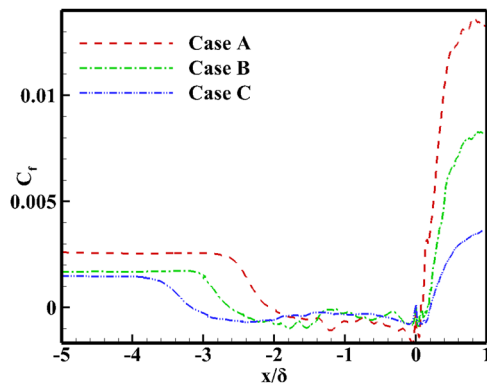**FIG. 5.** Distribution of the skin friction coefficient in the corner region where the horizontal coordinates are normalized by δ (δ is the boundary layer thickness).
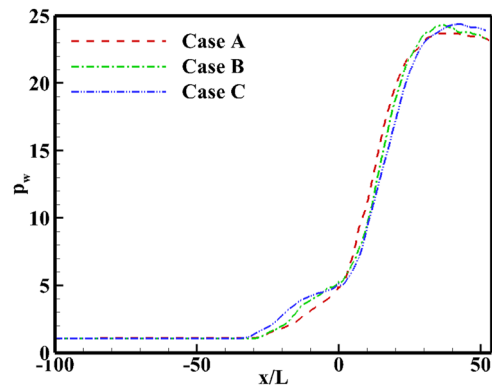

FIG. 7. Wall pressure p_w for different cases.

It is obvious that the increased Reynolds number would lead to early transition. In addition, the figures also show that the increased Reynolds number would decrease the value of the skin friction and the heat flux. We also show distribution of the skin friction coefficient in the corner region, where the horizontal coordinates are normalized by δ (δ is the boundary layer thickness) in Fig. 5. From the figure, we can see that the separation bubble is larger as the Reynolds number increases. The reason for the larger separation bubble will be discussed in Subsection IV B. As the Reynolds number continues to increase, there is a critical value. If the Reynolds number is larger than the critical value, the length of the separation bubble will decrease as the the Reynolds number increases. However, that is not discussed in this paper.

Figure 6 shows the mean Van Driest transformed velocity profile at x = −120 mm for different cases. As shown in the figure, the values for different cases are almost same at $y^+ < 10$. At $y^+ > 10$, the value of the mean velocity profile would increase as the Reynolds number increases.
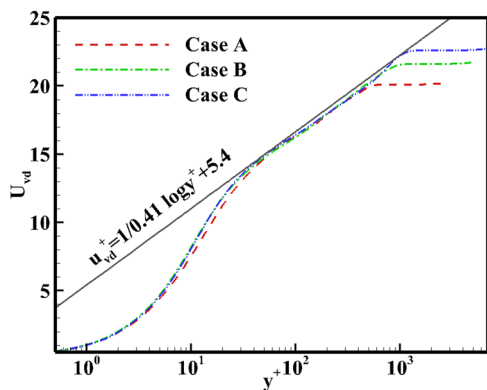
Figure 7 shows the wall pressure pw for different cases. We can know that the pressure increases at x/L > −30 and there are platforms at −30 < x/L < 0. As the Reynolds number increases, the value of the platform becomes larger. That means the separation becomes more obvious.

Through the frequency spectrum analysis,[30] we show the spectra of pressure fluctuations for case A at x/L = −100, y/L = 1, and z/L = 10 in Fig. 8. From the figure, we can know that the turbulence is fully developed.

We also show the instantaneous temperature at the x-y plane for different cases in Fig. 9. From the figures, we know that the temperature in the separation bubble becomes higher when the Reynolds number increases. We also show the instantaneous density gradient at the x-y plane for different cases in Fig. 10. From the figures, it can be seen that there are more shocklets at −30 < x/L < 0 in cases B and C than in case A. To see the separation shock clearly, the averaged density gradients at the x-y plane for different cases are shown in Fig. 11. In Fig. 11, it is clearly seen that the separation shock becomes stronger as the Reynolds number increases. Thus,
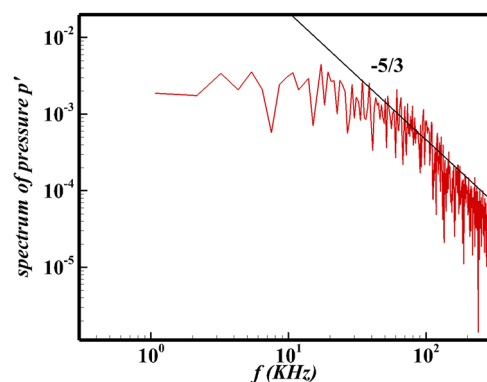

FIG. 6. Mean Van Driest transformed velocity profile at x = −120 mm for different cases.

FIG. 8. Spectra of pressure fluctuations for case A at x/L = −100, y/L = 1, and z/L = 10.
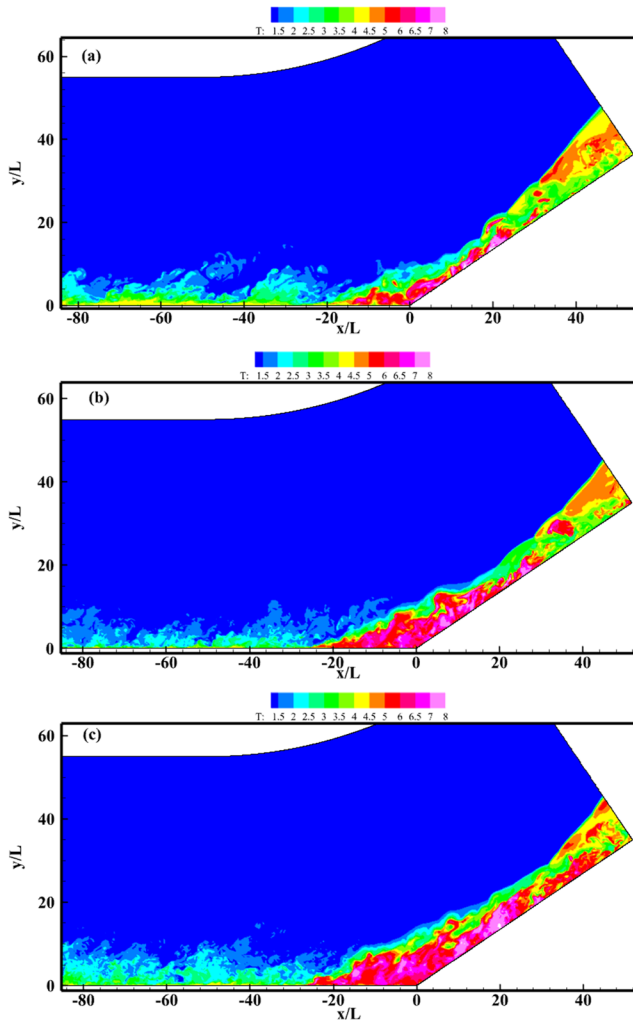
FIG. 9. Instantaneous temperature at the x-y plane for different cases. (a) is for case A; (b) is for case B; (c) is for case C.
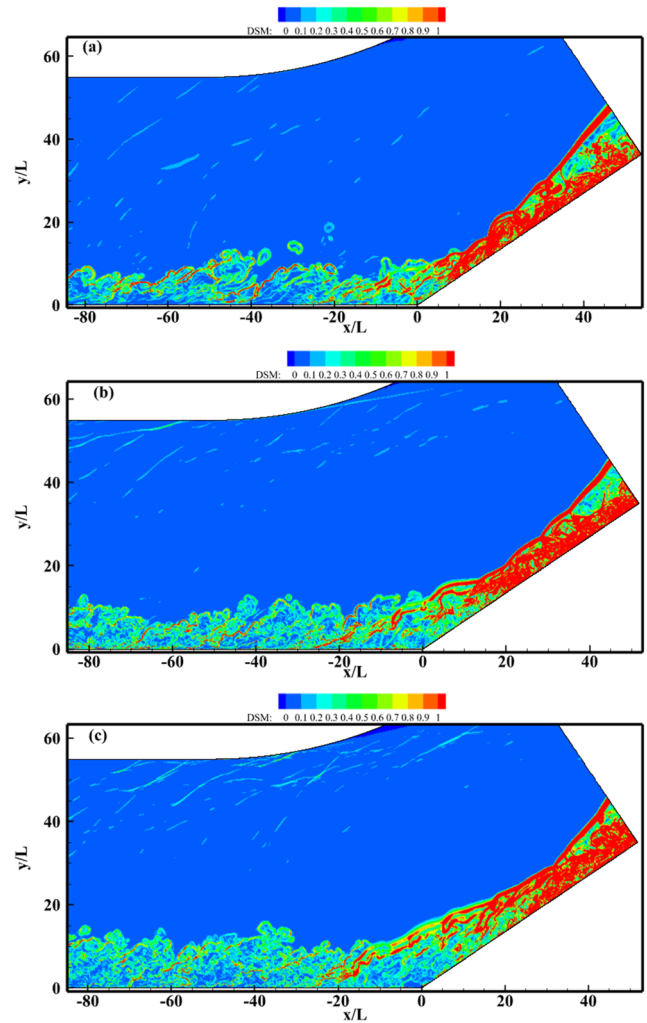

FIG. 10. Instantaneous density gradient (DSM) at the x-y plane for different cases. (a) is for case A; (b) is for case B; (c) is for case C.

we can deduce that the higher Reynolds number would strengthen the separation shock, which would lead to a larger separation bubble. The numerical schlieren image at the x-y plane for different cases is shown in Fig. 12, and from the figures, we can see the structures more clearly. The methods for density gradients and numerical schlieren can be found in Ref. 26.

The instantaneous isosurface of Q = 0.1 (second invariant of the strain rate tensor) for case A is shown in Fig. 13. From Fig. 13, we can find that the flow structures from the corner regime are more than those from the plate regime.

B. Decomposition of the mean skin-friction drag

The mean skin-friction drag can be decomposed into different physics-informed contributions based on the mean and statistical turbulence quantities across the wall layer. For the flat flow, from the filtered N–S equations, the mean skin-friction drag[31] can be decomposed as

$$
C_f = \underbrace{\frac{2}{\rho_\infty u_\infty^3} \int_0^\delta \langle \tau_{yx} \rangle \frac{\partial \{\tilde{u}\}}{\partial y} dy}_{C_{f1}} + \underbrace{\frac{2}{\rho_\infty u_\infty^3} \int_0^\delta \langle \bar{\rho} \rangle \{-\tilde{u}''\tilde{v}''\} \frac{\partial \{\tilde{u}\}}{\partial y} dy}_{C_{f2}}
$$

$$
+ \underbrace{\frac{2}{\rho_\infty u_\infty^3} \int_0^\delta \langle \bar{\rho} \rangle (\{\tilde{u}\} - u_\infty) \frac{D\{\tilde{u}\}}{Dt} dy}_{C_{f3}}
$$

$$
- \underbrace{\frac{2}{\rho_\infty u_\infty^3} \int_0^\delta (\{\tilde{u}\} - u_\infty) \frac{\partial}{\partial x} (\langle \tau_{xx} \rangle - \langle \bar{\rho} \rangle \{\tilde{u}''\tilde{u}''\} - \langle \bar{p} \rangle) dy}_{C_{f4}},
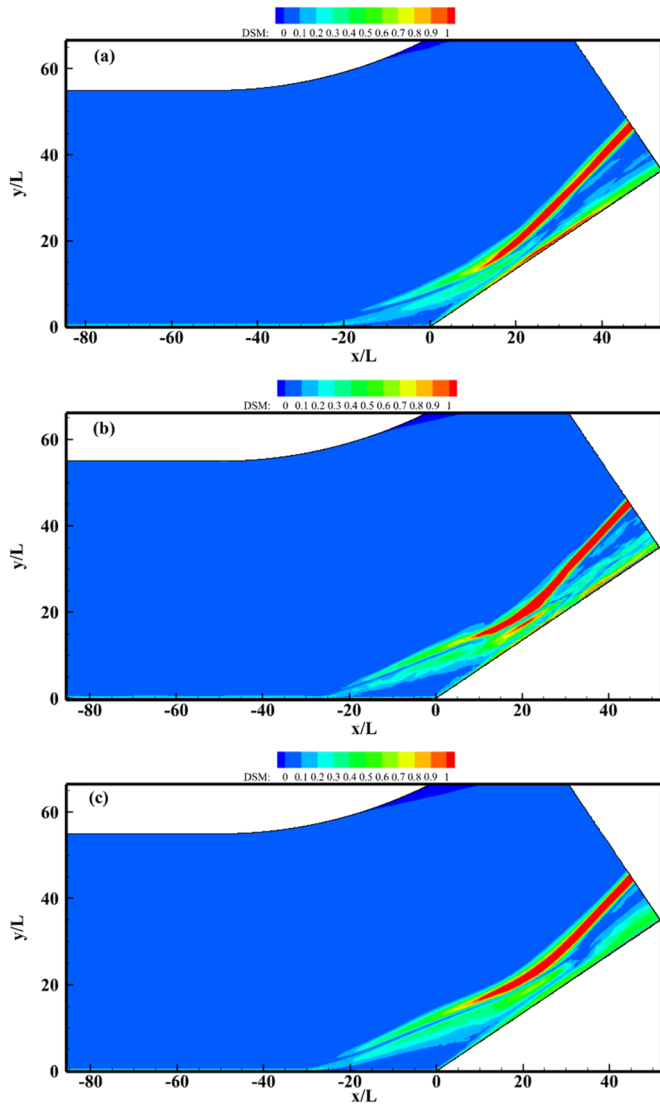$$

$$(31)$$

FIG. 11. Averaged density gradient (DSM) at the x-y plane for different cases. (a) is for case A; (b) is for case B; (c) is for case C.

where $\langle \cdot \rangle$ is the Reynolds averaging operator, $\{ \cdot \}$ is the Favre average ($\{\tilde{\phi}\} = \langle \bar{\rho}\tilde{\phi} \rangle / \langle \bar{\rho} \rangle$), and the double prime $''$ denotes the turbulent fluctuations with respect to the Favre average, i.e., $\tilde{\phi}'' = \tilde{\phi} - \{\tilde{\phi}\}$, u_∞ is the free-stream velocity, ρ_∞ is the free-stream density, τ_{xx} is the normal stress in the x-direction, and τ_{yx} is the shear stress in the streamwise direction. In addition, $D\{\cdot\}/Dt$ denotes that $D\{\cdot\}/Dt = \partial\{\cdot\}\partial t + \{v\}(\partial\{\cdot\}/\partial y)$.

In Eq. (31), C_{f1} represent the direct viscous dissipation, and C_{f2} represents turbulence "dissipation" into turbulent kinetic-energy production. C_{f3} represents the variation in the mean streamwise kinetic energy with time; C_{f4} is created by the streamwise heterogeneity. In the following, C_{f1} and C_{f2} will be discussed. After the inflection point (x = 0 mm), we also show the decomposed mean skin-friction drag as
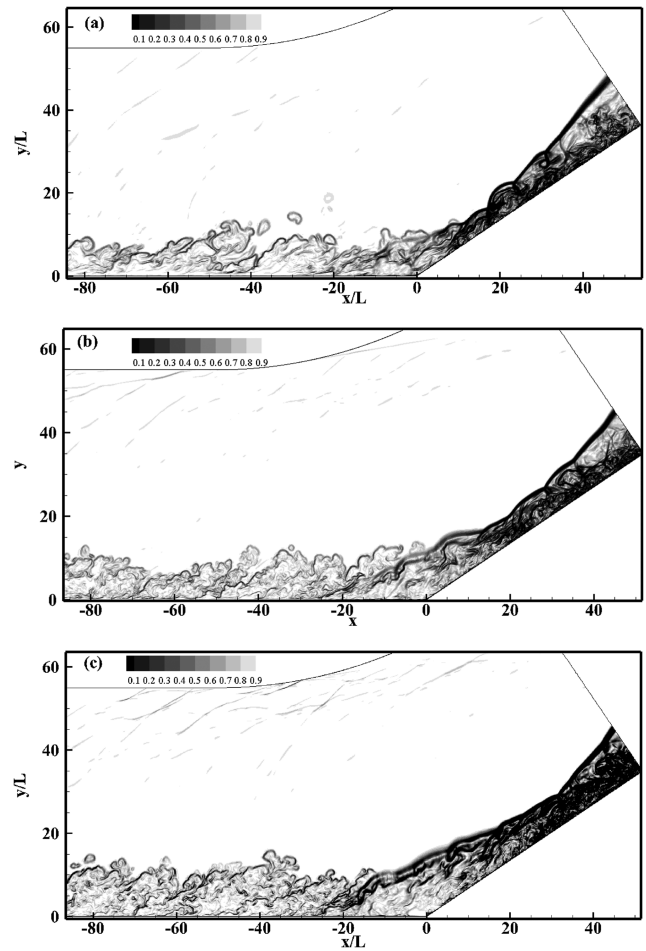

FIG. 12. Numerical schlieren image at the x-y plane for different cases. (a) is for case A; (b) is for case B; (c) is for case C.

$$C_f = \underbrace{\frac{2}{\rho_\infty u_\infty^3} \int_0^\delta \langle \tau_{yx} \rangle \frac{\partial \{\tilde{u}_n\}}{\partial y_n} dy_n}_{C_{f1}} + \underbrace{\frac{2}{\rho_\infty u_\infty^3} \int_0^\delta \langle \bar{\rho} \rangle \{ -\tilde{u}_n'' \tilde{v}_n'' \} \frac{\partial \{\tilde{u}_n\}}{\partial y_n} dy_n}_{C_{f2}}$$

$$+ \underbrace{\frac{2}{\rho_\infty u_\infty^3} \int_0^\delta \langle \bar{\rho} \rangle (\{\tilde{u}_n\} - u_\infty \cos\theta) \frac{D\{\tilde{u}_n\}}{Dt} dy_n}_{C_{f3}}$$

$$- \underbrace{\frac{2}{\rho_\infty u_\infty^3} \int_0^\delta (\{\tilde{u}_n\} - u_\infty \cos\theta) \frac{\partial}{\partial x_n} (\langle \tau_{xx} \rangle - \langle \bar{\rho} \rangle \{\tilde{u}_n'' \tilde{u}_n'' \} - \langle \bar{p} \rangle) dy_n}_{C_{f4}},$$

$$(32)$$

where $x_n = x\cos\theta$, $y_n = y\cos\theta$, $u_n = u\cos\theta + v\sin\theta$, and $v_n = u\sin\theta + v\cos\theta$. θ is the deflection angle of the corner, and $\theta = 34°$.

Figure 14 shows the terms C_{f1} and C_{f2}, which are dimensionless by C_f at $-30 < x/L < 10$. Figure 15 shows the terms C_{f1} and C_{f2}, which are dimensionless by C_f at $5 < x/L < 35$. From the figures, we can know that C_{f1} increases as the Reynolds number decreases for
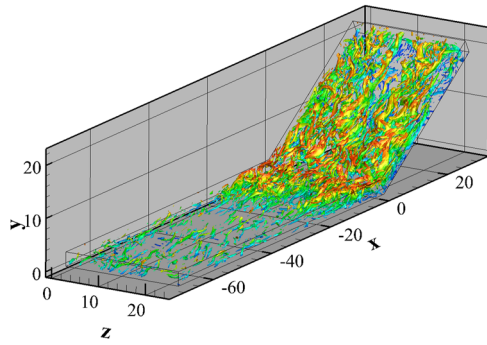
08 April 2024 03:10:27

FIG. 13. Instantaneous isosurface of Q = 0.1 (second invariant of the strain rate tensor) for case A.

both $-30 < x/L < 0$ and $5 < x/L < 35$. Thus, we know that the direct viscous dissipation is lower with the increasing Reynolds number. In addition, we can see that C_{f2} increases as the Reynolds number increases at $-30 < x/L < 0$ but C_{f2} decreases with the increasing Reynolds number at $5 < x/L < 35$. We can know that the production of turbulent kinetic energy by the turbulent dissipation is lower after reattachment with a higher Reynolds number while turbulent kinetic energy production by the turbulent dissipation becomes larger as the Reynolds number increases at the interaction region. We can also
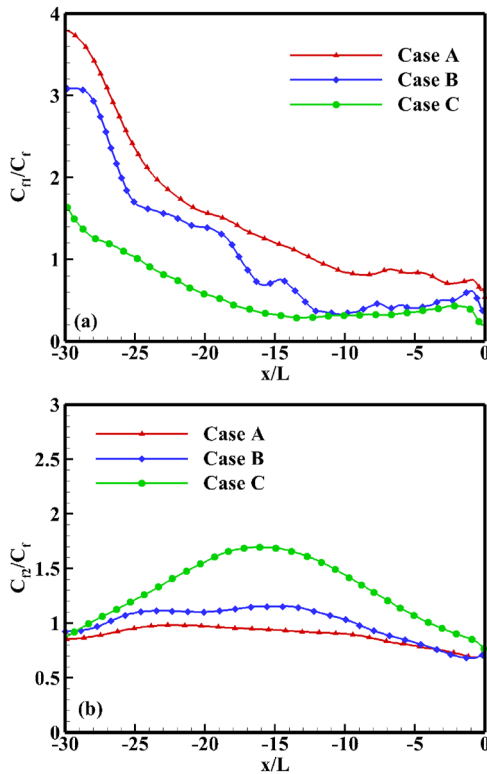

FIG. 14. Terms C_{f1} and C_{f2}, which are dimensionless by C_f at $-30 < x/L < 0$. (a) The term C_{f1}; (b) the term C_{f2}.
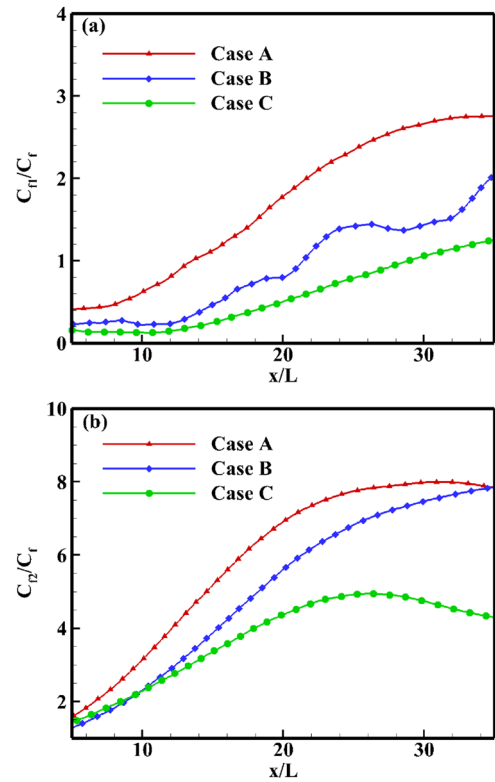

FIG. 15. Terms C_{f1} and C_{f2}, which are dimensionless by C_f at $5 < x/L < 35$. (a) The term C_{f1}; (b) the term C_{f2}.

know that for the case of a higher Reynolds number, high turbulent kinetic energy inhibits the movement of the separation point to the inflection point. There are some similar conclusions for the movement of the separation point in Ref. 32. Thus, the separation bubble of case A is larger than that of case B and case C.

V. CONCLUSION AND DISCUSSION

In this paper, the interaction between a shock wave and the hypersonic turbulent boundary layer in a compression corner with a fixed 34° deflection angle at Ma = 6 using large-eddy simulation for three different Reynolds numbers is carried out. The validation of the data is provided by showing the rms compared with others. The mean velocity, the wall skin-friction, the wall heat flux, and the wall pressure are shown. The distribution of the temperature and the shock wave is also studied. The decomposition of the mean skin-friction drag for both the flat-region and the corner region is determined. Through this research, some conclusions are provided:

(1) By comparing three cases of different Reynolds numbers, we know that the separation bubble length becomes larger and the separation shock wave is further away from the interaction region as the Reynolds number increases. In addition, the temperature in the interaction region is larger when the Reynolds number is larger.

(2) Through the decomposition of the mean skin-friction drag, we know that higher Reynolds numbers would increase the turbulent kinetic energy by turbulent dissipation at the interaction region while higher Reynolds numbers would decrease the turbulent kinetic energy by turbulent dissipation after reattachment. The reason for the larger separation bubble length is that the turbulent kinetic energy is larger with higher Reynolds numbers and higher turbulent kinetic energy inhibits the movement from the separation point to the inflection point (x = 0 mm).

ACKNOWLEDGMENTS

AUTHOR DECLARATIONS

Conflict of Interest

The authors have no conflicts to disclose.

Author Contributions

Han Qi (齐涵): Conceptualization (equal); Data curation (equal); Formal analysis (equal); Investigation (equal); Methodology (equal); Software (equal); Visualization (equal); Writing – original draft (equal). **Xinliang Li (李新亮)**: Data curation (equal); Funding acquisition (equal); Resources (equal); Software (lead). **Xiangxin Ji (纪相鑫)**: Software (equal); Validation (equal). **Fulin Tong (童福林)**: Conceptualization (equal); Formal analysis (equal); Investigation (equal); Methodology (equal). **Changping Yu (于长平)**: Funding acquisition (equal); Investigation (equal); Methodology (equal); Writing – original draft (equal); Writing – review & editing (equal).

DATA AVAILABILITY

The data that support the findings of this study are available from the corresponding author upon reasonable request.

TABLE III. The grid setting for grid convergence.

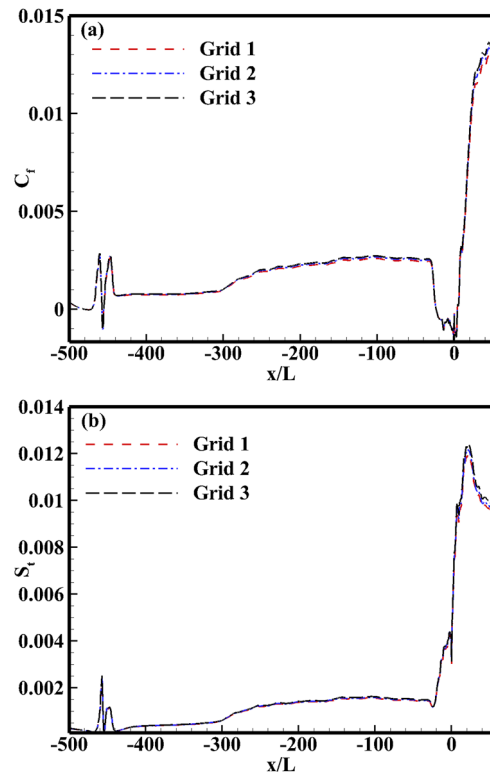| Case	Grids
Grid 1	$2200 \times 300 \times 250$
Grid 2	$2500 \times 300 \times 250$
Grid 3	$2500 \times 400 \times 300$

FIG. 16. Grid convergence for case A. (a) is the mean wall-skin friction; (b) is the Stanton number.

APPENDIX: GRID CONVERGENCE

In this section, we will show the grid convergence for case A. We supply three different grid settings, and the grid settings can be found in Table III. Figure 16 shows the mean wall-skin friction and the Stanton number for different grid settings. In the figures, we can see that the results are close, and we can infer that the grid converges.

REFERENCES

[1] D. S. Dolling, "Fifty years of shock-wave/boundary-layer interaction research: What next?," AIAA J. **39**, 1517–1530 (2001).

[2] D. V. Gaitonde, "Progress in shock wave/boundary layer interactions," Prog. Aerosp. Sci. **72**, 80–99 (2015).

[3] J. R. Edwards, "Numerical simulations of shock/boundary layer interactions using time dependent modeling techniques: A survey of recent results," Prog. Aerosp. Sci. **44**, 447–465 (2008).

[4] D. Knight, J. Longo, D. Drikakis, D. Gaitonde, A. Lani, I. Nompelis, B. Reimann, and L. Walpot, "Assessment of CFD capability for prediction of hypersonic shock interactions," Prog. Aerosp. Sci. **48–49**, 8–26 (2012).

[5] D. S. Dolling, "High-speed turbulent separated flows: Consistency of mathematical models and flow physics," AIAA J. **36**, 725–735 (1998).

[6] N. A. Adams, "Direct simulation of the turbulent boundary layer along a compression ramp at $M = 3$ and $Re_\theta = 1685$," J. Fluid Mech. **420**, 47–83 (2000).

[7] S. Pirozzoli and F. Grasso, "Direct numerical simulation of impinging shock wave/turbulent boundary layer interaction at $M = 2.25$," Phys. Fluids **18**, 065113 (2006).

08 April 2024 03:10:27

[8]M. Wu and M. P. Martin, "Direct numerical simulation of supersonic turbulent boundary layer over a compression ramp," AIAA J. **45**, 879–889 (2007).

[9]P. Bookey, C. Wyckham, A. Smits, and M. Martin, "New experimental data of STBLI at DNS/LES accessible Reynolds numbers," in *43rd AIAA Aerospace Sciences Meeting and Exhibit* (American Institute of Aeronautics and Astronautics, Reno, NV, 2005).

[10]M. Wu and M. P. Martín, "Analysis of shock motion in shock wave and turbulent boundary layer interaction using direct numerical simulation data," J. Fluid Mech. **594**, 71–83 (2008).

[11]S. Priebe and M. P. Martín, "Low-frequency unsteadiness in shock wave-turbulent boundary layer interaction," J. Fluid Mech. **699**, 1–49 (2012).

[12]C. Helm, M. Martin, and P. Dupont, "Characterization of the shear layer in a Mach 3 shock/turbulent boundary layer interaction," J. Phys.: Conf. Ser. **506**, 012013 (2014).

[13]J. Fang, Y. Yao, A. A. Zheltovodov, Z. Li, and L. Lu, "Direct numerical simulation of supersonic turbulent flows around a tandem expansion-compression corner," Phys. Fluids **27**, 125104 (2015).

[14]X. Li, D. Fu, and Y. Ma, and X. Liang, "Direct numerical simulation of shock/turbulent boundary layer interaction in a supersonic compression ramp," Sci. China, Ser. G: Phys., Mech. Astron. **53**, 1651–1658 (2010).

[15]A. Zheltovodov, "Shock waves/turbulent boundary-layer interactions–fundamental studies and applications," AIAA Paper 1996-1977, 1996.

[16]M. S. Loginov, N. A. Adams, and A. A. Zheltovodov, "Large-eddy simulation of shock-wave/turbulent-boundary-layer interaction," J. Fluid Mech. **565**, 135–169 (2006).

[17]G. Muzio, F. Peter, S. Hickel, and N. Adams, "Large-eddy simulation of a supersonic turbulent boundary layer over a compression-expansion ramp," Int. J. Heat Fluid Flow **42**, 79–93 (2013).

[18]C. S. Combs, J. D. Schmisseur, B. F. Bathel, and S. B. Jones, "Unsteady analysis of shock-wave/boundary-layer interaction experiments at Mach 4.2," AIAA J. **57**, 4715–4724 (2019).

[19]Z. Sun, T. Gan, and Y. Wu, "Shock-wave/boundary-layer interactions at compression ramps studied by high-speed schlieren," AIAA J. **58**, 1681–1688 (2020).

[20]Z. Feng-Yuan, "Hypersonic shock wave/turbulent boundary layer interaction over a compression ramp," AIAA J. (published online, 2023).

[21]P. Stephan and M. M. Pino, "Turbulence in a hypersonic compression ramp flow," Phys. Rev. Fluids **6**, 034601 (2021).

[22]X. Chai and K. Mahesh, "Dynamic k-equation model for large-eddy simulation of compressible flows," J. Fluid Mech. **699**, 385–413 (2012).

[23]H. Qi, X. Li, R. Hu, and C. Yu, "Quasi-dynamic subgrid-scale kinetic energy equation model for large-eddy simulation of compressible flows," J. Fluid Mech. **947**, 32 (2022).

[24]F. Tong, X. Li, J. Duan, and C. Yu, "Direct numerical simulation of supersonic turbulent boundary layer subjected to a curved compression ramp," Phys. Fluids **29**, 125101 (2017).

[25]M. P. Martín, E. M. Taylor, M. Wu, and V. G. Weirs, "A bandwidth-optimized WENO scheme for the effective direct numerical simulation of compressible turbulence," J. Comput. Phys. **220**, 270–289 (2006).

[26]J. Duan, X. Li, X. Li, and H. Liu, "Direct numerical simulation of a supersonic turbulent boundary layer over a compression–decompression corner," Phys. Fluids **33**, 065111 (2021).

[27]S. Pirozzoli, F. Grasso, and T. B. Gatski, "Direct numerical simulation and analysis of a spatially evolving supersonic turbulent boundary layer at M = 2.25," Phys. Fluids **16**, 530–545 (2004).

[28]S. Pirozzoli and M. Bernardini, "Turbulence in supersonic boundary layers at moderate Reynolds number," J. Fluid Mech. **688**, 120–168 (2011).

[29]X. Wu and P. Moin, "Direct numerical simulation of turbulence in a nominally zero-pressure-gradient flat-plate boundary layer," J. Fluid Mech. **630**, 5–41 (2009).

[30]X. Li, D. Fu, and Y. Ma, "Direct numerical simulation of hypersonic boundary layer transition over a blunt cone with a small angle of attack," Phys. Fluids **22**, 025105 (2010).

[31]W. Li, Y. Fan, D. Modesti, and C. Cheng, "Decomposition of the mean skin-friction drag in compressible turbulent channel flows," J. Fluid Mech. **875**, 101–123 (2019).

[32]F. Tong, X. Li, Z. Tang, X. Zhu, and J. Huang, "Transition effect on separation bubble of shock wave/boundary layer interaction in a compression ramp," Acta Aeronaut. Astronaut. Sin. **37**, 2909–2921 (2016).

08 April 2024 03:10:27